

Numerical methods for particle simulations at extreme densities and temperatures: Weighted particles, relativistic collisions and reduced currents

Y. Sentoku^{a,*}, A.J. Kemp^b

^a *University of Nevada, Reno, Department of Physics, Reno, NV 89506, United States*

^b *Lawrence Livermore National Laboratory, Livermore, CA 94551, United States*

Received 3 April 2007; received in revised form 28 March 2008; accepted 28 March 2008

Available online 14 April 2008

Abstract

We present a fully relativistic energy-conserving binary collision model for particle simulations with large density scale plasmas. Our model deals with collisions between weighted particles of arbitrary species, conserving energy perfectly in each collision while momentum is conserved on the average. We also discuss a new method to model extremely high densities, applicable to a wide range of plasmas from the cold, non-relativistic to the ultra-relativistic regime in the high energy density physics.

© 2008 Elsevier Inc. All rights reserved.

Keywords: PIC; Binary collision; Weighted particles

1. Introduction

Recent advances in the development of intense short pulse lasers have led to exciting progress in high energy density physics (HEDP). As an example, a several μm thin foil that is irradiated by a 100 TW, sub-pico-second laser pulse reaches keV ($1\text{ keV} \approx 11,000,000\text{ }^\circ\text{C}$) temperatures at solid density, while the electron distribution is temporarily far out of equilibrium, featuring two or more widely distinct temperatures. In modeling such extreme plasmas, both kinetic- and collisional-effects on the energy transport are essential. A particular difficulty is the large density gradients between critical density n_c and solid density exceeding several hundreds of n_c . The critical density is the density where the laser is absorbed and $n_c = 10^{21}\text{ cm}^{-3}$ for a $1\text{ }\mu\text{m}$ wavelength pulse. This means that a numerical model needs to describe the laser–plasma interaction in the low density region, as well as fast particle transport in the extremely dense target region where Coulomb collision processes are important for energy transfer. In the fast-ignitor scheme of laser fusion [1], the density scale covers five orders of magnitude from the laser interaction region to the compressed core. Another

* Corresponding author.

E-mail address: sentoku@physics.unr.edu (Y. Sentoku).

example for a naturally occurring plasma with large density gradients is the ionosphere of our planet, in particular the polar outflow where the ion density changes by more than two orders of magnitude. Under such conditions, simulations can be done more efficiently with using weighted particles than with using uniform weighted particles, because huge number of particles are necessary in dense region in the case with uniform particles otherwise we end up bad statistics in the low density plasmas. While being standard practice for kinetic simulations, the use of weighted particles is less straightforward for the description of collisions. This is one topic of the present article. Another difficulty arises from the extreme plasma densities in laser–solid interaction or in the fast-ignitor scheme. Below we will describe a method that is designed to suppress numerical instabilities. While we focus on a description of the numerical method, the implications for the physics will be discussed elsewhere.

A binary Coulomb collision algorithm in cases where each particle represents the same fraction of the particle density has been first presented by Shanny et al. [2], and extended to multi-component plasma by Takizuka and Abe (1977) [TA77] for plasma simulations [3]. In TA77 both momentum and energy are conserved perfectly for non-relativistic kinematics. Later, TA77 has been extended to relativistic kinematics and tested in the weakly relativistic regime by one of the authors [4]. Miller and Combi have developed an algorithm for weighted particle simulations employing Monte-Carlo techniques [5]. Their model has been generalized to arbitrary particle weights by Nanbu and Yonemura (1998) [NY98] [6]. In the latter approach, momentum and energy are not always conserved in each individual collision, but macroscopically they are conserved on the average. This is permissible as long as there are enough particles, which is generally the case in Monte-Carlo simulations, but in typical HEDP Particle-in-Cell (PIC) simulations [7] the number of particle per cell tends to be small (<100) for reasons of computational cost, resulting in an unacceptable violation of energy/momentum conservation. Note that it is not possible to conserve both energy and momentum in collisions between differently weighted particles exactly by modifying the equilibration rates, but ignoring the weights in the collision kinematics. This leads to inaccurate modeling of bulk properties due to the local violation of energy/momentum conservation. We introduce a technique to improve this problem.

The collision model described here is purely kinematic in nature, i.e. quantum effects are included only through the limits for the impact parameter that enter the Coulomb logarithm. Effects, like the emission of bremsstrahlung radiation by fast charged particles in matter, are not included at this point. One can estimate the ratio of radiation losses to collisional losses for an electron with energy $\gamma m_e c^2$ in a material with atomic charge Z as $dE_{\text{rad}}/dE_{\text{coll}} \approx \alpha Z \gamma$, where α is a constant coefficient. This ratio becomes unity, namely, the radiation will become significant against the collisional-effect for an electron in air with $\gamma \approx 200$ and 20 in lead [8, Chapter 15]. This means that one can neglect radiation losses for laser-accelerated electrons at energies below 20 MeV. In Section 3.2, we show how radiation effects compare to collisional ones for a hydrogen plasma (Fig. 4).

2. Relativistic binary collision model between weighted particles

We first present an advanced Coulomb collision model for small angle scattering between weighted particles with fully relativistic kinematics. Our model features perfect energy conservation in individual collisions and momentum conservation on the average, which is a great advantage for HEDP simulations in which the numerical heating or energy violation must be very small to get an accurate laser energy coupling to plasmas. After presenting the model, several test simulations are performed to demonstrate its validity.

2.1. Relativistic binary collision model

We begin by introducing a fully relativistic binary collision model for small angle Coulomb scattering. Pairs of particles undergoing binary collisions are determined at random in each spatial cell. In PIC simulations, for which this model was conceived, the simulation grid size should ideally coincide with the Debye length so that one performs collisions between particles in a Debye sphere. This is consistent with the physical model of collisions in a plasma. However, for all practical purposes the collision cell size only needs to be smaller than typical density- and temperature-gradient lengths, while being large enough to provide good statistics for

the collision operator. Apart from this, the result of the collision operator should be independent of the cell size. Note that the computational cost of a TA77 type collision operator scales with the number of particles N , as opposed to a full Boltzmann description of binary collisions which scales with N^2 .

The pairing procedures between particles are identical to TA77, and energy and momentum exchanges are calculated for each pair, performed in the center-of-momentum (CM) frame of the two particles. Details are described in Ref. [4]. Here we revise the calculation of the scattering angle in Ref. [4] by following strictly relativistic kinematics in order to make the model applicable to the ultra-relativistic regime.

2.1.1. Center-of-momentum frame

The kinematics of a relativistic collision between two particles with masses m_α and m_β and four-momenta $(p_\alpha^0, \mathbf{p}_\alpha)^T$ and $(p_\beta^0, \mathbf{p}_\beta)^T$ is best described in the center-of-momentum frame of reference (CM). Note that it is not affected by the weight of the particles, as will be discussed below. The CM velocity is given by

$$\mathbf{v}_{\text{CM}} = \frac{\mathbf{p}_\alpha + \mathbf{p}_\beta}{p_\alpha^0 + p_\beta^0}, \quad \gamma_{\text{CM}} = \frac{1}{\sqrt{1 - \mathbf{v}_{\text{CM}}^2/c^2}}. \quad (1)$$

The momenta $\mathbf{p}_{\alpha,\beta}$ as given in the laboratory frame of reference (LAB) are transformed into the CM frame by a Lorentz transformation [8, Chapter 11]

$$p_\alpha^0 = \gamma_{\text{CM}}(p_\alpha^0 - \mathbf{v}_{\text{CM}} \cdot \mathbf{p}_\alpha) \quad (2)$$

$$\mathbf{P}_\alpha = \mathbf{p}_\alpha + \frac{\gamma_{\text{CM}} - 1}{v_{\text{CM}}^2}(\mathbf{v}_{\text{CM}} \cdot \mathbf{p}_\alpha)\mathbf{v}_{\text{CM}} - \gamma_{\text{CM}}p_\alpha^0\mathbf{v}_{\text{CM}}. \quad (3)$$

Accordingly, for each particle $\gamma_{\alpha,\text{CM}} \equiv P_\alpha^0/m_\alpha$, and velocities are $\mathbf{V}_\alpha = \mathbf{P}_\alpha/(m_\alpha\gamma_{\alpha,\text{CM}})$. The CM frame is defined by

$$\mathbf{P}_\alpha + \mathbf{P}_\beta = 0, \quad (4)$$

and throughout the collision process total momentum is conserved, i.e. the magnitude of momentum of each particle is invariant

$$|\mathbf{P}_\alpha| = |\mathbf{P}_\beta| = |\mathbf{P}'_\alpha| = |\mathbf{P}'_\beta| = P, \quad (5)$$

where P is the momentum amplitude.

The relative velocity between the two particles in the CM frame, required for the calculation of the collision frequency, is given by

$$\mathbf{v}_{\text{rel}} = \frac{\mathbf{V}_\alpha - \mathbf{V}_\beta}{1 - \mathbf{V}_\alpha \cdot \mathbf{V}_\beta/c^2}. \quad (6)$$

For the description of the scattering process in the code, we rotate the coordinate system of momentum space to the system in which the P_z -axis is aligned with the momentum vector \mathbf{P}_α of the first particle. This transformation is represented by

$$\begin{pmatrix} \cos \theta_R \cos \phi_R & \cos \theta_R \sin \phi_R & -\sin \theta_R \\ -\sin \phi_R & \cos \phi_R & 0 \\ \sin \theta_R \cos \phi_R & \sin \theta_R \sin \phi_R & \cos \theta_R \end{pmatrix} \begin{pmatrix} P_x \\ P_y \\ P_z \end{pmatrix} = \begin{pmatrix} 0 \\ 0 \\ P \end{pmatrix}. \quad (7)$$

Here θ_R is the angle between P_z -axis and the vector \mathbf{P}_α , and ϕ_R is the angle between P_x – P_z plane, where P_x -, P_y - and P_z -axis are for the CM frame. The inverse matrix calculation of Eq. (7) will be done after scattering to rotate back to the CM frame. Note that the majority of the computer time consumed by the binary collision operator is spent by randomizing and pairing particles, and not by calculating the collision kinematics.

2.1.2. Scattering angle in the CM frame

In the relativistic regime, the frequency of small angle scattering between particle species with charges e_α and e_β is given by [10],

$$v_{\alpha\beta} = \frac{4\pi(e_\alpha e_\beta)^2 n_l L}{p_{\text{rel}}^2 v_{\text{rel}}}, \quad (8)$$

where $v_{\text{rel}}(p_{\text{rel}})$ is the relative velocity (momentum) between two particles. In the relativistic case, however, it is defined as the velocity of one-particle in the rest frame of the other. We call this frame the one-particle-at-rest (OPR) frame in the following discussion. e_α and e_β are the charge of each particle, n_l is the lower density among n_α and n_β . The Coulomb logarithm is defined as $L = \log(1/\theta_{\min})$, where θ_{\min} is the smallest angle for which the process can still be regarded as small angle Coulomb scattering. It is related to the distance of closest approach between the two charges, namely the impact parameter b . In the classical case, θ_{\min} is the scattering angle for which b is equal to the Debye length λ_D . The corresponding transverse momentum transfer $q \sim |e_\alpha e_\beta|/\lambda_D v_{\text{rel}}$. Dividing q by the longitudinal momentum $p_{\text{rel}} = m_{\alpha\beta} v_{\text{rel}}$, we find $\theta_{\min} \sim |e_\alpha e_\beta|/\lambda_D m_{\alpha\beta} v_{\text{rel}}^2$, and $L = \log(\lambda_D m_{\alpha\beta} v_{\text{rel}}^2/|e_\alpha e_\beta|) \sim \log(\lambda_D^3 n_l)$, where $m_{\alpha\beta}$ is the reduced mass. The condition for classical scattering is that $|e_\alpha e_\beta|/\hbar v_{\text{rel}} \gg 1$, here \hbar is the Planck constant.

This condition is not satisfied in the relativistic case, so that the scattering must be treated quantum-mechanically using the Born approximation [9]. Here the scattering cross-section is expressed in terms of the Fourier component of the scattering potential with wave vector q/\hbar . Now that minimum scattering angle θ_{\min} is found from $q_{\min} \lambda_D/\hbar \sim p_{\text{rel}} \theta_{\min} \lambda_D/\hbar \sim 1$. In this case, then, $L = \log(\lambda_D p_{\text{rel}}/\hbar)$ is expressed as the ratio of the Debye length and the de Broglie wave length. Note here that $|e_\alpha e_\beta| \sim \hbar v_{\text{rel}}$ corresponds to $T_e \sim 15$ eV for e–e collisions, so that we work in the Born approximation most of the time. Certainly, the expressions for the Coulomb logarithm in the classical and quantum limits coincide at this threshold. Note here that in the calculation of the Coulomb logarithm, we are not evaluating the background temperature. The relative energy $m_{\alpha\beta} v_{\text{rel}}^2$ is used as a temporal temperature, assuming that the averaged quantity would be close to the background temperature through a lot of samplings. Also the correct Coulomb logarithm for stopping power actually involves the fast particle velocity instead of the relative velocity [11]. Because we use the relative velocity as the general formula, we have about a factor 2 difference in the logarithmic scale. Nevertheless, since it stands in a logarithm, the resulting error is insignificant as shown in our test calculations. Having one general formula for stopping and relaxation problems is useful for realistic problems, such as the laser–plasma interaction, which has both the fast particle stopping and thermalization simultaneously.

To avoid a divergence of the collision frequency in cold plasma we have set a threshold for a degenerate plasma [12]. The transition temperature T_0 from the Spitzer regime to the degenerate regime is calculated by the condition

$$\frac{T_0}{m_e c^2} = \left(\frac{\sqrt{2} \pi^{3/2} \hbar^3 n_h}{m_e^{3/2}} \right)^{2/3}, \quad (9)$$

at which the Spitzer collision frequency equals the one in the degenerate regime. Here n_h is the higher density among n_α and n_β . A collision with less energy than T_0 is treated as a collision in degenerate plasmas. The collision frequency is then constant

$$v_{\alpha\beta} = \frac{4m_e Z e^4 L}{3\pi \hbar^3}. \quad (10)$$

After calculating $v_{\alpha\beta}$ for a given pair of particles, the scattering angle θ , greater than 0, is chosen randomly from a Gaussian distribution with variance

$$\langle \tan^2(\theta/2) \rangle = v_{\alpha\beta} N_c \Delta t, \quad (11)$$

where the Δt is the time step and N_c is the number of time steps between subsequent sampling times for calculation of the collision. This choice warrants that the resulting collision term is equal to that of a Fokker–Planck equation [2]. Note that θ is the scattering angle of the projectile particle in the OPR frame. We limit the right hand side of Eq. (11) to 1/50. This means that the average scattering angle should be small in each time step. This restriction assures that our model is close to multiple small angle scattering based on the central limit theorem, which has a Gaussian distribution of scattering angles with a minimum scattering variance [8, Chapter 13]. By excluding large angle scattering, we improve the phase space of particles with the limited

number of particles per cell in simulations, since larger angle scattering would diffuse the phase space statistically worse, especially in weighted particle simulations.

Since the momentum transfer is easily calculated in the center-of-momentum (CM) frame, θ is transferred to the CM frame. After scattering in OPR, the momentum P' and the energy ϵ' in the CM are obtained by the Lorentz transformation

$$\begin{pmatrix} \epsilon' \\ \mathbf{P}' \end{pmatrix} = \begin{pmatrix} \gamma_{\text{cm}} & -\beta_{\text{cm}}\gamma_{\text{cm}} \cdot \mathbf{I} \\ -\beta_{\text{cm}}\gamma_{\text{cm}} \cdot \mathbf{I} & \gamma_{\text{cm}} \end{pmatrix} \begin{pmatrix} \epsilon_{\text{L}} \\ \mathbf{P}_{\text{L}} \end{pmatrix}, \quad (12)$$

where β_{cm} is the reduced velocity of the CM system, and γ_{cm} is the Lorentz factor of the system. ϵ_{L} , $\mathbf{P}_{\text{L}} \equiv (0, P_{\text{L}} \sin \theta, P_{\text{L}} \cos \theta)$ is the energy and the momentum of the projectile particle after the collision in the OPR frame, respectively. Note here that P_{L} and ϵ_{L} are not calculated because of the complexity in the momentum and energy transfer in the OPR frame. We will do that in the CM frame after obtaining the scattering angle θ_{cm} in the CM frame as described below. We assume here that the particle run along the z -axis before collision for simplicity. Then,

$$\begin{pmatrix} \epsilon' \\ 0 \\ P' \sin \theta_{\text{cm}} \\ P' \cos \theta_{\text{cm}} \end{pmatrix} = \begin{pmatrix} \gamma_{\text{cm}} \epsilon_{\text{L}} - \beta_{\text{cm}} \gamma_{\text{cm}} P_{\text{L}} \cos \theta \\ 0 \\ P_{\text{L}} \sin \theta \\ -\beta_{\text{cm}} \gamma_{\text{cm}} \epsilon_{\text{L}} + \gamma_{\text{cm}} P_{\text{L}} \cos \theta \end{pmatrix}. \quad (13)$$

Eliminating P' , we have a relation of θ_{cm} and θ ,

$$\tan \theta_{\text{cm}} = \frac{\sin \theta}{\gamma_{\text{cm}} (\cos \theta - \beta_{\text{cm}}/\beta)}, \quad (14)$$

where β is the reduced velocity after scattering in the OPR frame. Since β is not calculated yet, we used the initial velocity to evaluate Eq. (14). Because we are treating the small angle scattering only, the energy transfer rate is small and also the reduced velocity does not change much through collision in the relativistic case, this approximation is justified. For the electron–ion collision, since $m_e \ll M$, $\beta_{\text{cm}} \sim 0$ and $\gamma_{\text{cm}} \sim 1$, the scattering angle in the CM, $\tan \theta_{\text{cm}}$, is approximately $\tan \theta$. For the electron–electron collision in the non-relativistic regime, $\beta_{\text{cm}} = \beta/2$ and $\gamma_{\text{cm}} \sim 1$ make $\tan \theta_{\text{cm}} \sim 2 \tan \theta$, which agrees the classical scattering angular relation. In the relativistic electron–electron collision, the scattering angle θ_{cm} is more than two times larger than θ due to the relativistic gamma effects.

2.1.3. Scattering process

Throughout each binary collision, the magnitude of the momentum P is constant, only its direction is changed:

$$(0, 0, P) \rightarrow (P \sin \theta_{\text{cm}} \cos \phi_{\text{cm}}, P \sin \theta_{\text{cm}} \sin \phi_{\text{cm}}, P \cos \theta_{\text{cm}}), \quad (15)$$

where the azimuthal angle ϕ_{cm} is uniformly distributed in the interval $[0, 2\pi]$. Then the momentum change of the particle in the collision is given in the CM frame by the inverse rotation of Eq. (7), i.e.

$$\begin{pmatrix} \Delta P_x \\ \Delta P_y \\ \Delta P_z \end{pmatrix} = \begin{pmatrix} \cos \theta_R \cos \phi_R & -\cos \theta_R \sin \phi_R & \sin \theta_R \\ \sin \phi_R & \cos \phi_R & 0 \\ -\sin \theta_R \cos \phi_R & -\sin \theta_R \sin \phi_R & \cos \theta_R \end{pmatrix} \begin{pmatrix} P \sin \theta_{\text{cm}} \cos \phi_{\text{cm}} \\ P \sin \theta_{\text{cm}} \sin \phi_{\text{cm}} \\ P \cos \theta_{\text{cm}} \end{pmatrix} - \begin{pmatrix} P_x \\ P_y \\ P_z \end{pmatrix}. \quad (16)$$

By using $\Delta \mathbf{P} = (\Delta P_x, \Delta P_y, \Delta P_z)$, we get the momentum after the collision,

$$\mathbf{P}'_{\alpha} = \mathbf{P}_{\alpha} + \Delta \mathbf{P}, \quad (17)$$

$$\mathbf{P}'_{\beta} = \mathbf{P}_{\beta} - \Delta \mathbf{P}. \quad (18)$$

Finally, the particle momenta in the laboratory frame are obtained by

$$\mathbf{p}'_{\alpha} = \mathbf{p}_{\alpha} + \frac{\gamma_{\text{CM}} - 1}{v_{\text{CM}}^2} (\mathbf{v}_{\text{CM}} \cdot \mathbf{p}'_{\alpha}) \mathbf{v}_{\text{CM}} + \gamma_{\text{CM}} P_{\alpha}^0 \mathbf{v}_{\text{CM}}. \quad (19)$$

These calculations will be done for each binary pair.

2.2. Collisions between weighted particles

For simulations of particle transport in large density gradients, weighted particles are not only more efficient than uniformly weighted ones but in some cases necessary due to limits of computer memory. Using an appropriate pairing statistics, the Coulomb collision operator described in TA77 can be extended to weighted particles. The scattering calculation is identical to the one described in the previous section. The key difference to the TA77 operator is the fact that the heavier of the two particles is scattered with a finite probability. Let us first describe the weighted particle collision operator presented in NY98 [6].

Let $w_{\alpha i}$ represent the weight of the i th particle of species α , and similarly, $w_{\beta j}$ is for j th particle of species β . The number density of each species in a cell is then given by

$$n_{\alpha} = \sum_i w_{\alpha i}, \quad n_{\beta} = \sum_j w_{\beta j}. \quad (20)$$

When the i th particle of species α collides with the j th particle of species β , the simulated particle α_i undergoes a collision with probability $P_{\alpha} = w_{\beta j} / \max(w_{\alpha i}, w_{\beta j})$ and the particle β_j does with probability $P_{\beta} = w_{\alpha i} / \max(w_{\alpha i}, w_{\beta j})$. For example, $w_{\alpha i} = 2$, $w_{\beta j} = 6$, particle α_i does collide with $P_{\alpha} = 1$, means α_i is scattered always. On the other hand, β_j does $P_{\beta} = 2/6$, which means that particle β_j scattered in two of six collisions. By generating an uniformly distributed random number r , ($0 \leq r < 1$), particle β_j is scattered only when $r < P_{\beta}$, reflecting the scattering probability; if $r > P_{\beta}$ particle β_j is not scattered. The idea of this so-called ‘rejection’ method is illustrated in Fig. 1a. It is a common Monte-Carlo simulation technique [5]. However, this approach does not conserve energy and momentum in each individual collision. This works well when $N_{\text{cell}} \gg 10^3$. But with $N_{\text{cell}} \leq 100$ the statistic of energy conservation is unacceptable. Note that particle weights are not included in the momentum transfer calculation described in the previous section to treat differently weighted particles as particles of the defined species.

We propose an alternative way of scattering the heavier particle in which both the light particle α_i and the heavy one β_j are always scattered, while β_j undergoes only partial scattering depending on the scattering probability P_{β} as illustrated in Fig. 1b. In particular, only $P_{\beta} w_{\beta}$ sub-particles in β_j are scattered. After that, the heavier particle’s energy and momentum are merged in the particle β_j by the following steps for energy,

$$\epsilon_{\beta}^{\text{after}} = \epsilon_{\beta}^{\text{before}} \cdot (1 - P_{\beta}) + \epsilon_{\beta}^{\text{scattered}} \cdot P_{\beta}, \quad (21)$$

and for momentum,

$$\mathbf{p}_{\beta}^{\text{after}} = \mathbf{p}_{\beta}^{\text{before}} \cdot (1 - P_{\beta}) + \mathbf{p}_{\beta}^{\text{scattered}} \cdot P_{\beta}. \quad (22)$$

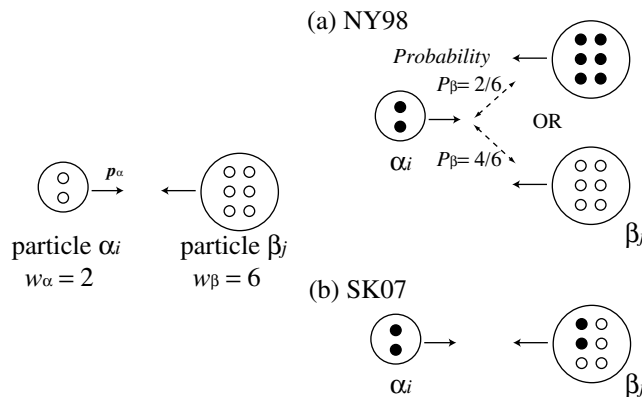


Fig. 1. Collision between weighted particles. (a) NY98: rejection method; (b) SK07: merging method.

We know that after these calculations, both energy and momentum “before” are conserved, but the momentum p_{β}^{after} is not consistent with the energy $\epsilon_{\beta}^{\text{after}}$ anymore. The energy calculated based on the scattered momentum p_{β}^{after} in this way is smaller than the particle energy given by Eq. (21). So we lose the momentum somewhere in the merging process. In a physical sense, the collided particles and the rest do a quick thermalization in a macro-particle, so that their “internal energy” increases.

To correct for this loss in energy, we add a perpendicular momentum to the p_{β}^{after} as a thermal momentum,

$$\mathbf{p}_{\beta}^{\text{final}} = \mathbf{p}_{\beta}^{\text{after}} + \Delta \mathbf{p}_{\beta\perp}. \quad (23)$$

The magnitude of $p_{\beta\perp}$ is calculated such that energy is conserved. Since this $p_{\beta\perp}$ is chosen in the plane perpendicular to $\mathbf{p}_{\beta}^{\text{after}}$ and pointing randomly in that plane, the total momentum is conserved *on the average*. The thermal momentum is calculated by the following equation,

$$\Delta |p_{\perp}| = m_{\beta} c \sqrt{\gamma_{\epsilon_{\beta}^{\text{after}}}^2 - \gamma_{p_{\beta}^{\text{after}}}^2}, \quad (24)$$

where

$$\gamma_{\epsilon_{\beta}^{\text{after}}} = 1 + \epsilon_{\beta}^{\text{after}} / m_{\beta} c^2, \quad (25)$$

$$\gamma_{p_{\beta}^{\text{after}}} = \sqrt{1 + |p_{\beta}^{\text{after}}|^2 / m_{\beta} c^2}. \quad (26)$$

In NY98, there is another important idea of a common time increment per real particle in the weighted particle collision. When the number of macro-particle in a cell, $N_{\alpha} > N_{\beta}$, the number of binary collisions is N_{α} , and the total number of collision of real particles through the binary collisions is

$$n_{\alpha\beta} = \sum_i^{N_{\alpha}} \frac{w_{\alpha i} w_{\beta i}}{\max(w_{\alpha i}, w_{\beta i})}. \quad (27)$$

To make the total number of collision of real particles equal to the case with uniformly weighted particles, we adjust the time step by multiplying a factor,

$$\Delta t = \frac{n_{\alpha}}{n_{\alpha\beta}} \Delta t_0. \quad (28)$$

This is a common time increment per real particle. Here Δt_0 is the simulation time step. When $N_{\beta} > N_{\alpha}$, we use $\Delta t = (n_{\beta} / n_{\alpha\beta}) \Delta t_0$.

We illustrate an example of these processes in Fig. 2 to show this time adjustment idea more clearly. These two cases show the same system (the same number of real particles), but it is described by the different manner.

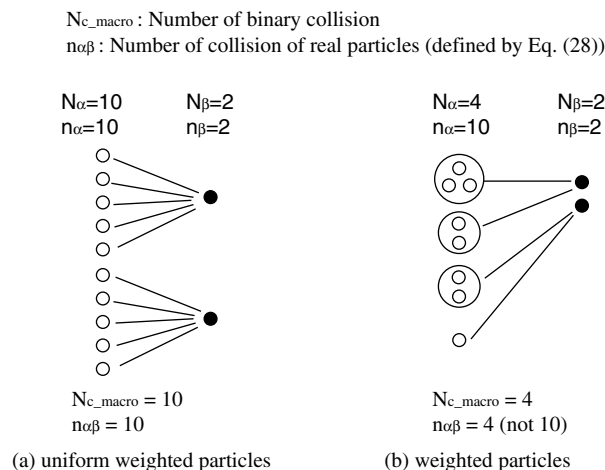


Fig. 2. Sample cases: (a) with uniform weighted particles; (b) weighted particles.

‘Real’ particle means a particle which has a standard weight. In Case (a) of collisions with uniformly weighted particles between species α and β , we have 10 binary collisions and also 10 real particle collisions. On the other hand, Case (b) for weighted particle collisions has only four binary collisions. The number of real particles which were collided is $n_{\alpha\beta} = 4$. To adjust the total number of collision of real particles to make identical to Case (a), the time step of Case (b) was adjusted by Eq. (28), $\Delta t = (10/4) \cdot \Delta t_0$. Since $v\Delta t$ represents the number of events of collision in a time step Δt , the number of collision between real particles of Case (b) becomes statistically identical to the one of Case (a) through this process.

In the case of α and β are identical, the number of collision is $N = N_\alpha/2$ for even N_α , and $N_\alpha = (N_\alpha + 1)/2$ for odd N_α . The number of real particles that have collided is

$$n_{\alpha\alpha} = 2 \sum_i^N \frac{w_{2i-1}w_{2i}}{\max(w_{2i-1}, w_{2i})}, \quad (29)$$

where a factor 2 comes from two particles identity. Then we can choose $\Delta t = (n_\alpha/n_{\alpha\alpha})\Delta t_0$ as the simulation particle time step.

Since the number of collision of real particles in our model is the same in NY98, we do the same correction of the time step when we calculate Eq. (11).

3. Applications

3.1. Energy transfer rate in relativistic electron–ion collision

The first test problem is checking the energy transfer rate from relativistic electrons to ions. All electrons have the same initial energy but moving to randomly distributed direction: a shell distribution in momentum space. Taking into account that a shell distribution has a $\sqrt{\pi/2}$ times higher equilibration rate than the Maxwellian distribution, and expressing the energy by relativistic mechanics, we have the analytical exchange rate [9],

$$\frac{d(1 - E_i/E_e)}{dt} = \left(1 - \frac{E_i}{E_e}\right) \frac{8\pi z^2 e^4 n L}{M m_e c^3 (\gamma - 1)}. \quad (30)$$

The corresponding simulation is done with the following parameters: density 10^{26} cm^{-3} , ion mass $M = 1840 m_e$, the electrons initial energy was set from 2 keV to 10 MeV. A constant Coulomb $\log L = 5$ is used for simplicity. This simulation is performed as a pure Monte-Carlo simulation, omitting particle motion or EM fields. We chose extremely dense plasma not only to increase the energy transfer rate sufficiently high for convenience, but it is the parameter range of the fast ignition core. We did 1000 time steps then calculated the left hand side of Eq. (30) by evaluating the ion and electron total energy. Results are summarized in Fig. 3. The simulation reproduces the theoretical prediction Eq. (30) very well from the non-relativistic regime to relativistic regime. One simulation was performed with weighted particles, both electrons and ions have randomly distributed weights from 0 to 2, making the average weight ~ 1 . This weighted simulation is consistent with the theoretical prediction, too. This test also confirms that operating microscopic collisions by means of a Monte-Carlo methods can give the same results as using the macroscopic quantities, like the average density/energy as like expressed by Eq. (30).

3.2. Stopping power of relativistic electrons in plasma

Energetic electrons stopping power is calculated in a hydrogen plasma with a mass density $\rho = 12.5 \text{ g/cm}^3$ and the initial temperature 5 keV. Both electron–electron and electron–ion collisions are included, but the electron–electron collision is the dominant process in stopping. So this is a good benchmark for the electron–electron collision. Here we use 100 test particles and make them averaged to obtain the stopping power. Again, this simulation has been performed in a single cell. We did not solve the Maxwell equation in this simulation, namely, this is a pure Monte-Carlo simulation. We calculated the $\Delta E/(\ell\rho)$ in a first 100 time step, here ℓ is the distance the particle can proceed in 100 time step. Changing the initial electron energy from 10 keV to 1 GeV,

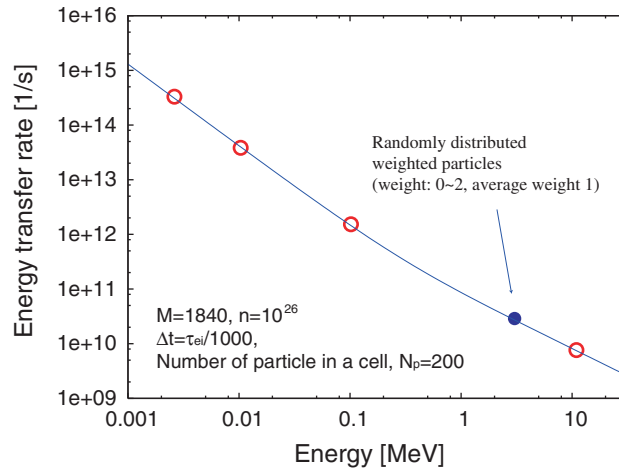


Fig. 3. Energy transfer rate between electrons and ions of mass M at density n . The line is calculated by Eq. (30). Open circles are simulation results with uniformly weighted particles. A solid circle indicate the result with weighted particles.

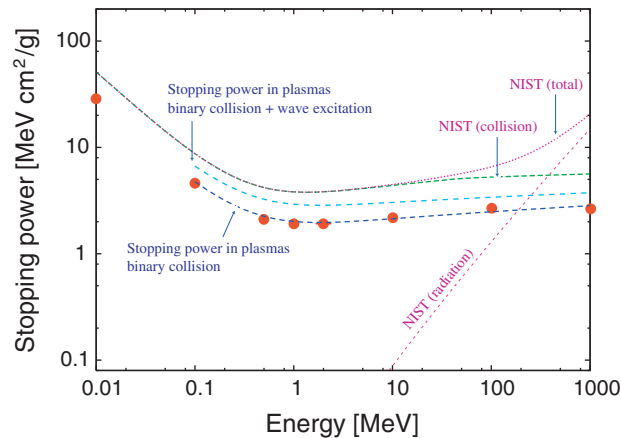


Fig. 4. Electron stopping power in hydrogen plasmas.

the stopping power is calculated and plotted in Fig 4 by solid circles. The stopping power in a hydrogen gas in NIST data base are also shown in Fig. 4 as a reference. Note here that the Coulomb logarithm in the NIST data is set by atomic physics while the plasma condition in our test. So the two cases are in different situation. Nevertheless, the computational results show the similar trend from the non-relativistic to the ultra-relativistic regime, except the radiation effect. The broken lines are the theoretical stopping power calculated by the Fokker–Planck equation without radiative stopping in a plasma [15]. The simulated stopping power marked by solid circles in Fig. 4 is reasonably agreed with the theoretical prediction for the binary collision in all energy ranges.

4. Beam relaxation: benchmark of the weighted particle collision model

The final test is a simulation of electron beam relaxation by the weighted collision model. Initially electrons have the Maxwellian distribution with thermal velocity $v_{th} = 0.001c$, where c is the speed of light, and 10% of the electrons drifting with a momentum $0.7m_e c$. The total electron density is 10^{25} cm^{-3} and only e–e collision was performed. This test is zero-dimensional in space and three-dimensional in velocity, i.e. our simulation was performed with one spatial cell. Again, this is purely a Monte-Carlo test.

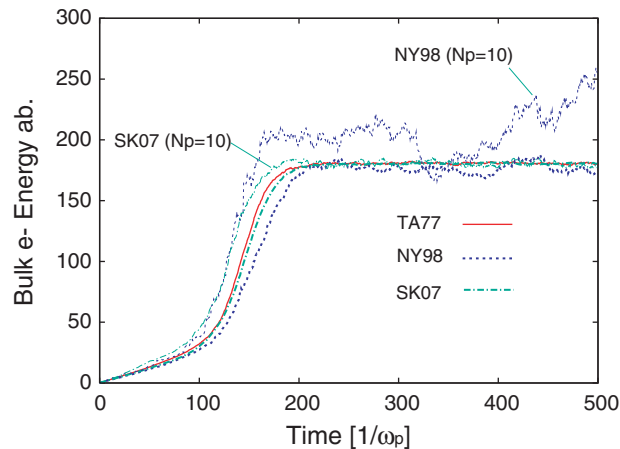


Fig. 5. Time history of the bulk electrons energy. Solid lines are obtained by TA77, broken lines are by NY98, and dot-and-broken lines are new scheme. Simulations with less number of particle (10 particles/cell) by NY98 and SK07 are also shown.

Since there is no energy input from the outside, the total energy must be conserved through the simulation. Simulations were performed with periodic boundaries with 10 cells by the three following models:

- Case A (TA77): uniform weighted particle, 500 particles/cell (bulk 450, drifting 50).
- Case B (NY98): weighted particle, 250 particles/cell (bulk 125, drifting 125) and 10 particles/cell (bulk 5, drifting 5).
- Case C (SK07; model described here): weighted particle, 250 particles/cell (bulk 125, drifting 125) and 10 particles/cell (bulk 5, drifting 5).

The case A is the uniform weighted simulation by TA77 and used here as a reference.

Fig. 5 shows the time evolution of the bulk electron energy. All three cases settle the same equilibrium energy, ~ 180 , and have almost the same slope before being saturated. Note here that NY98 is less accurate than our model due to violation of energy conservation. The total energy conservation is shown in Fig. 6a for the case of NY98 and SK07 with 10 particles/cell. The total energy of NY98 has fluctuating error and eventually exceeded 40%, which might be a serious problem in HEDP simulations. Both the TA77 and our model have perfect energy conservation through the simulation. The momentum conservation is also improved by our scheme as shown in Fig. 6b. We found that NY98 has about 5% error with 250 particles/cell and needs more than 500 per cell to get a better statistics.

The energy spectrum was also checked in three cases and the results are plotted in Fig. 7. The spectrum agrees well among them. These simulation results verify our approach in a treatment of the weighted particle collision by adding the thermal perpendicular momentum to conserve the energy. The good accuracy even with less number of particles is a great advantage for PIC simulations of HEDP.

5. Collisional reduced PIC model for large density scale plasma simulation

We have developed the collision model for weighted particles. Our model has the perfect energy conservation and the improved momentum conservation as discussed before. In this section, as an application of our collision model we would like to introduce an unique technique to simulate large density scale plasmas, which change the density from the kinetic to collisional regime. Such plasmas are important for the laser-plasma experiments, e.g., the fast ignition in the laser fusion, and the astrophysical objects research. Our Particle-in-Cell (PIC) code is PICLS, featuring a current-conserving integration scheme [16], a numerical dispersion-free Maxwell solver with the directional splitting scheme [7], which has been extended to the multi-dimensional problems. Also PICLS has a fourth order current/force interpolation to suppress the numerical instability causing under-resolving the Debye length. In general, it is challenging for PIC to simulate extremely

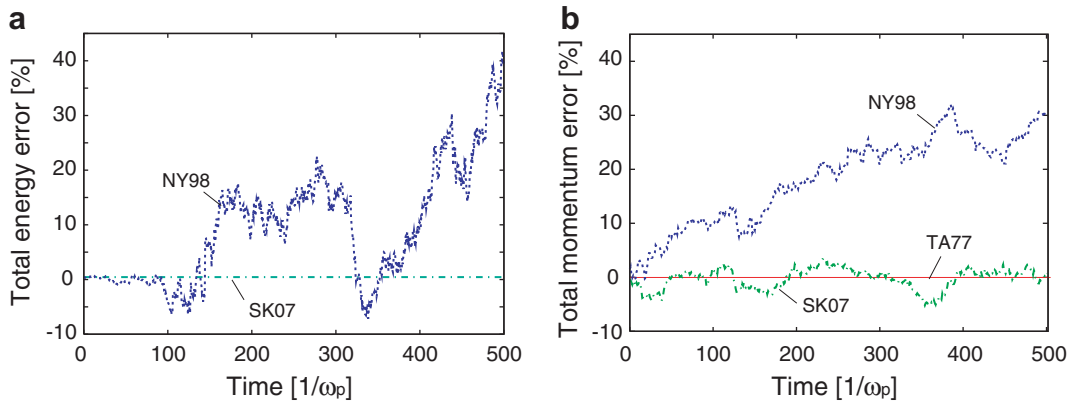


Fig. 6. Error of the total energy (a) and momentum (b) in the simulation with 10 particles/cell in the NY98 and the SK07 model.

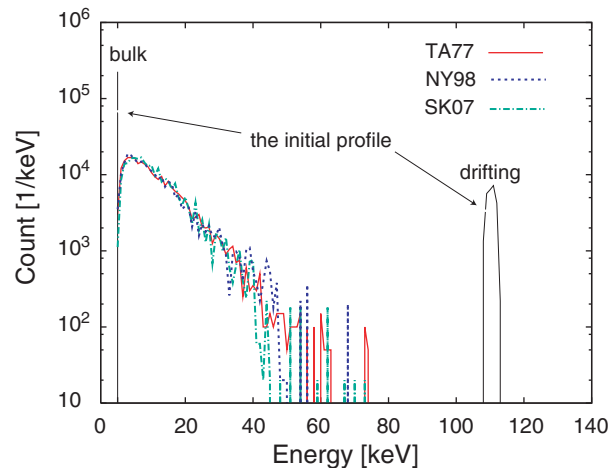


Fig. 7. Energy spectra of three cases at the end of the simulation, $t = 500$. NY98 and SK07 used 250 particles/cell.

dense and low temperature (less than 1 keV) plasmas, since the grid size of PIC is restricted by the plasma Debye length, $\propto \sqrt{T/n}$ to avoid the numerical heating. Therefore, a PIC simulation for such dense and low temperature plasmas requires huge number of grids (and also particles), and it is not realistic to perform even with the current fastest super computers. We have adapted a fourth order interpolation scheme to evaluate fields and currents to reduce the numerical heating while expanding grid size to \sim the plasma skin length. But still the computational cost is too expensive to simulate above a solid density plasmas, especially in multi-dimensional calculations.

We propose a “reduced PIC” technique to perform such large density scale plasmas to reduce the computational cost drastically. This concept is based upon the physics of the collisional damping of kinetic effects in dense plasmas [14]. The idea is illustrated in Fig. 8. Up to a certain density, here we call it n_{pic} , the kinetic physics is fully resolved alongside collisional process. Above the density n_{pic} , the kinetic physics becomes less important due to the collisional damping, and they are calculated with the reduced density n_{pic} . In this regime, the simulation becomes more like a Monte-Carlo calculation as plasma density increases. We have studied this threshold density and found that the kinetic physics will be damped at around $n_{\text{damp}} \sim 10^{23} \text{ cm}^{-3}$ in hydrogen plasmas at thermal temperatures under 1 keV [14]. Above that density n_{damp} , plasma waves are damped and the physics is dominated by collisional processes. Hence it is not necessary to resolve a small scale of the kinetic physics there. By setting n_{pic} greater than n_{damp} , we can make sure that all of the important kinetic physics are taken into account in the simulation. In the reduced PIC region, a particle located in a density

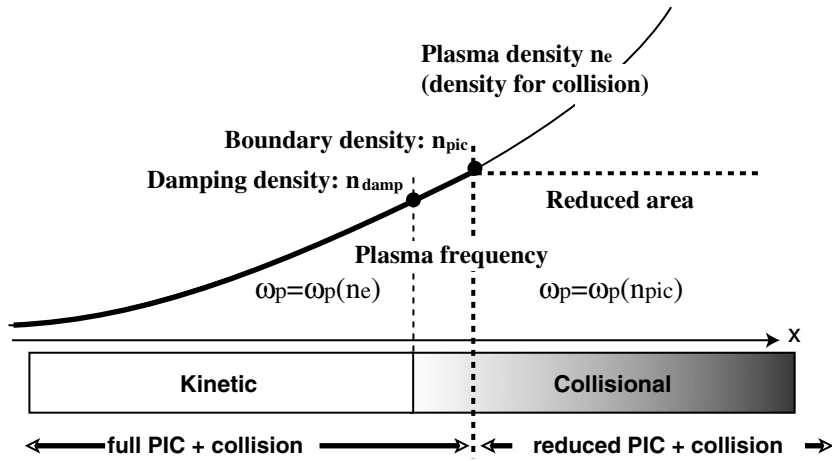
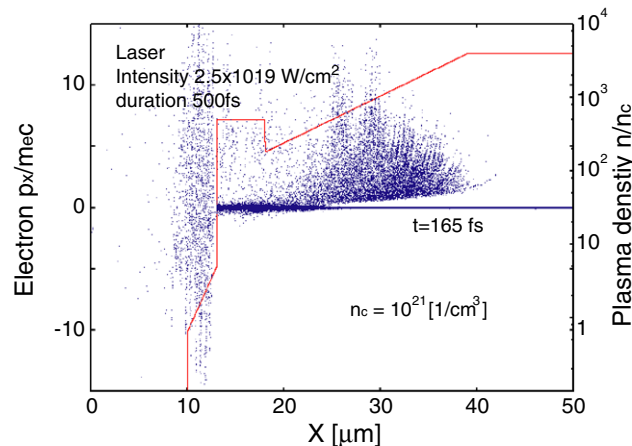


Fig. 8. Concept of the reduced PIC simulation along collisions.

n , which is higher than n_{pic} initially, is treated with a weight calculated by $w = w_0 \cdot n_{pic}/n_0$ in the PIC calculation, as a result, the plasma frequency above n_{pic} is treated as $\omega_p(n_{pic})$ in the kinetic physics. Here w_0 is the original particle weight. This treatment forces to satisfy the stability condition of the Maxwell solver, $\omega_p \Delta t < 2$ [13]. Note that for the collision operator the original particle weights are used to calculate the collision frequency in the real plasma density, and there is no charge build up due to this reducing treatment in the PIC calculation, because we implicitly check the divergence of E with charge density using the same current-conserving scheme. Our reduced PIC scheme is not versatile. One needs to consider the physical situation, especially about the collisional damping density, which might change dynamically with plasma heating. To produce reliable results, theoretical aspects like those mentioned in Ref. [14] are important for the target physics. Each initial result should be checked with higher resolved simulations.

In the following, we demonstrate the reduced PIC technique with a 1D simulation of an intense laser pulse interacting with a large density scale plasmas. The plasma density increases from $100n_c$ to $4000n_c$ behind the slab target which is placed to stop the laser light, see Fig. 9. We used this range of density because it includes the transition density from the kinetic to collisional regime even after the back ground plasmas were heated up to keV, which was predicted from Fig. 1 in Ref. [14]. The laser intensity is $2.5 \times 10^{19} \text{ W/cm}^2$ with duration 500 fs. The dense slab plasma placed at around 13–18 μm to stop the laser light and produce energetic elec-

Fig. 9. Density profile in the test of the reduced PIC technique. The density is normalized by the laser critical density n_c . (dots plot) The electron phase $X-p_x$ observed at 165 fs.

trons, which will travel through the large density plasmas as shown in Fig. 9. The maximum plasma density in the simulation is $4000n_c$. We performed two simulations, one by a fully resolved PIC simulation up to the maximum density. Here the “fully resolved PIC” means that it has a resolution of the plasma skin length ($c/\omega_p \sim 0.004 \mu\text{m}$) at the maximum density. The resolution used in the simulation is $\Delta x = 0.0025 \mu\text{m}$ and $\Delta t = 0.00833 \text{ fs}$. The other one is the reduced simulation with $n_{\text{pic}} = 600n_c$ with 2.5 times bigger grid and time step than the full resolved calculation. The “reduced” simulation has a resolution of the plasma skin length at n_{pic} , but under resolved the higher densities, while keeping the stability condition of the Maxwell solver $\omega_p(n_{\text{pic}})\Delta t < 2$. The both calculations used the same number of particle per cell, 200, initially and the density profile is prepared with weighted particles. The initial plasma temperature was set to $T_e = T_i = 150 \text{ eV}$. To cal-

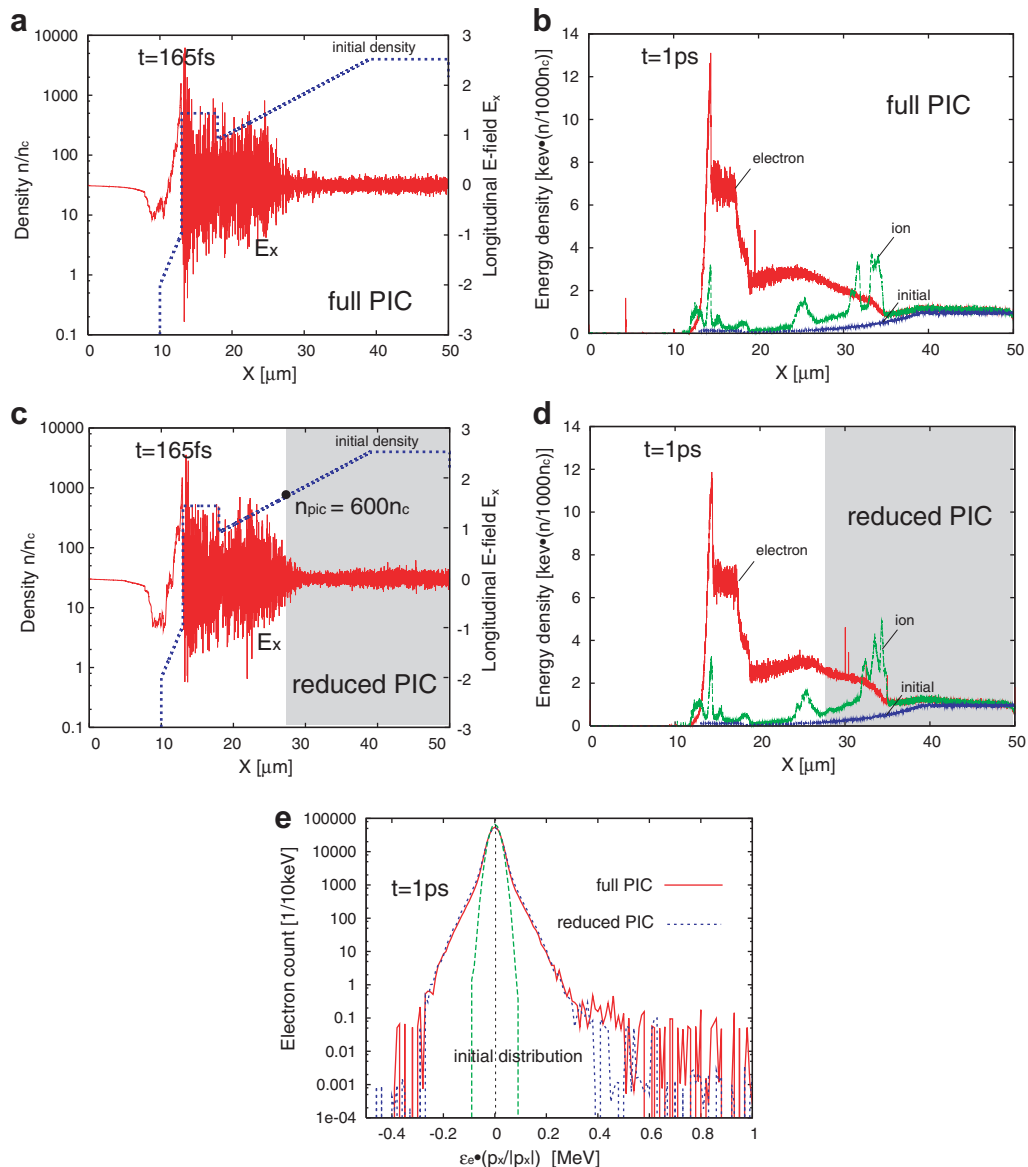


Fig. 10. (a) (full PIC) Longitudinal electric field at 165 fs. (b) (full PIC) Energy density of electrons and ions observed at 1 ps. (c) (reduced PIC) Longitudinal electric field at 165 fs. (d) (reduced PIC) Energy density of electrons and ions observed at 1 ps. (e) The energy spectrum comparison between full PIC (solid line) and reduced PIC (broken line). The spectrum was observed at 1 ps. The negative energy spectra show the energy distribution of particles flowing toward negative x -direction.

culate 1 ps, the full (reduced) PIC needs 120,000 (48,000) time steps. Note here that we suppress the numerical heating due to under-resolution of the Debye length of the initial temperature by adopting the fourth order interpolation in the PIC calculation. This high order interpolation makes the numerical heating much slower than the plasma heating via physical processes. In Fig. 10a and c shows the longitudinal electric field observed at 165 fs (during the laser irradiation). Both plots show the same trend. In the reduced PIC results, the reduced area is indicated with shading. The longitudinal fields are decaying at around $25\text{ }\mu\text{m}$, where the plasma density is a few hundred of the critical density. This damping density agrees well with the analytical prediction discussed in Ref. [14]. Both the electron and ion energy density plots also show the very good agreement between the two calculations. The energy spectra observed in the reduced area ($X > 30\text{ }\mu\text{m}$) are shown in Fig. 10e. This is observed at the same time with plot (b) and (d). We see very good agreements between two cases both in the high energy tail and bulk energy distribution. Based on these results, the reduced PIC simulation properly describes the energy transport and transfer physics in the extremely dense region.

Fig. 11 shows the spectrum of the longitudinal electric fields observed in the high density region ($n_e = 3200n_c$). We compare the spectra of a fully resolved simulation with and without collisions to one in which we use the reduced PIC algorithm. The spectra show how collisions damp plasma oscillations before the cutoff mode by about one order of magnitude, to a negligible level for the plasma heating. The energy of particles oscillating in those fields is about 50 eV in the case without collisions, and less than 1 eV with collisions. This means that the plasma is heated by the collisional processes dominantly, and not by plasma waves. Obviously the high frequency modes, which appear in the collisional, fully resolved simulation, are not resolved in the reduced calculation. Although we suppress these high frequency components in the reduced calculation, this is justified because they are not important for the heating processes.

Next, we demonstrate the reduced PIC technique in a two-dimensional problem. We performed a 2D simulation of an intense laser pulse interacting with a slab target. The laser intensity is $5 \cdot 10^{17}\text{ W/cm}^2$ with a $5\text{ }\mu\text{m}$ focus spot. A thin CD foil target with $5\text{ }\mu\text{m}$ thickness and $36\text{ }\mu\text{m}$ width is placed at the center of the simulation box. The target is initially fully ionized and its density is $1.6 \cdot 10^{23}\text{ cm}^{-3}$, which is 160 times greater than the critical density of the incident laser light. There is a pre-formed plasma in front of the target within $3\text{ }\mu\text{m}$. We perform two simulations; the first one is the fully resolved kinetic PIC simulation and the second is the reduced PIC simulation. Both cases include collisions. For the fully resolved kinetic calculation, we have 1000×2000 meshes with 72 million particles to resolve the skin length in the target. The mesh size is small enough to resolve the plasma skin length, $\Delta x = (1/6) \cdot c/\omega_p$ for $n_{\text{pic}} = 160n_c$. In the reduced PIC calculation, we reduced the number of meshes and particles to 500×1000 and 18 million, which is one quarter of the fully resolved kinetic simulation. The reduced calculation is 12 times faster than the fully resolved kinetic simulation. The target density of kinetic simulation is set four times less, $n_{\text{pic}} = 40n_c$. The damping density in these parameters is expected to be a few 10 critical density [14]. In a case of more intense laser irradiation, the damping density

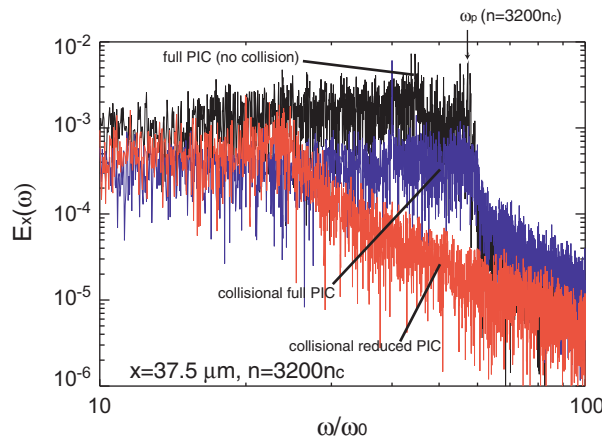


Fig. 11. Spectrum of longitudinal electric fields observed in the dense plasmas ($X = 37.5\text{ }\mu\text{m}$, $n = 3200n_c$).

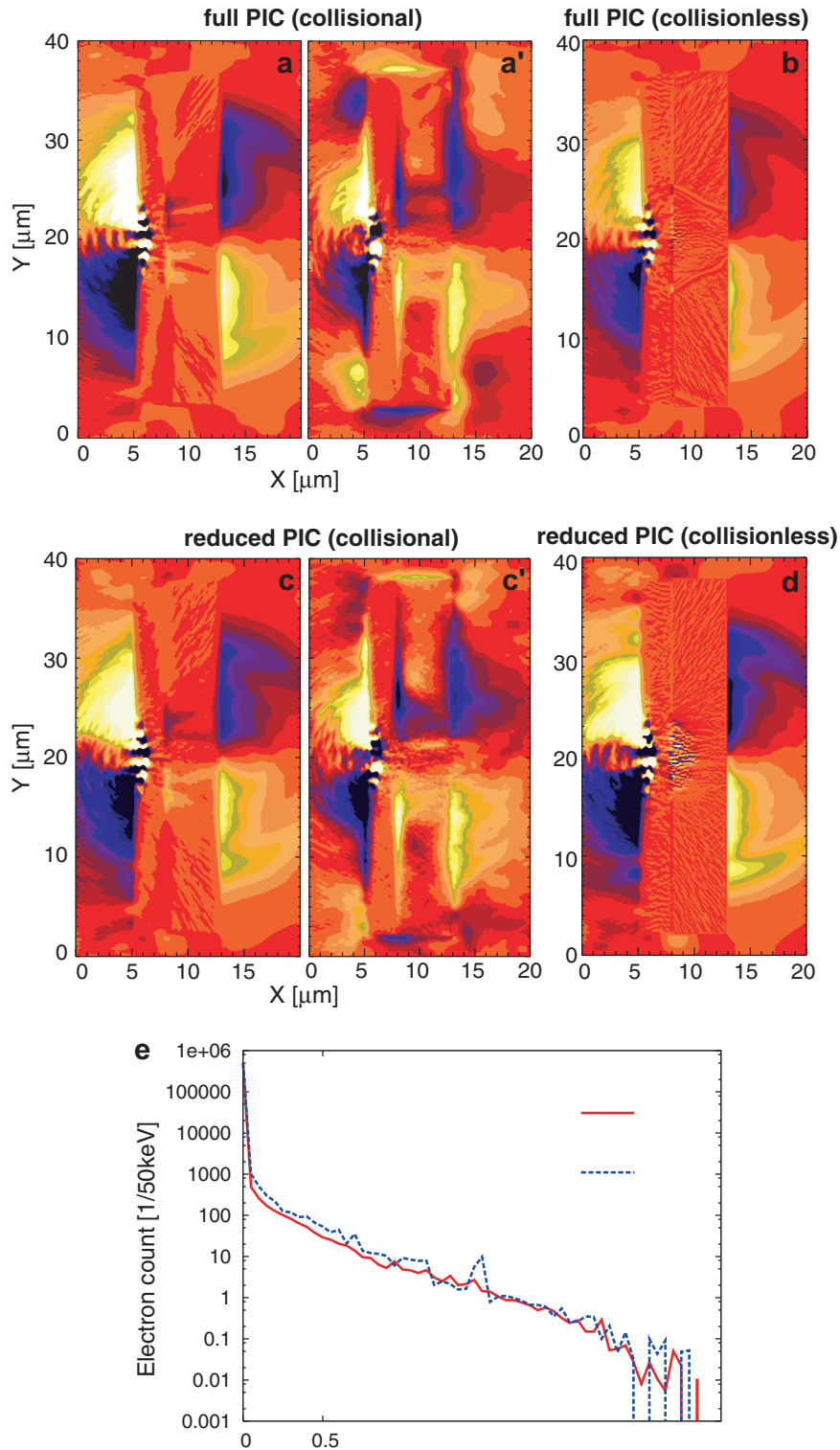


Fig. 12. Evolution of the quasi-static magnetic fields by the laser–foil interaction. (a) and (a') is the collisional fully resolved kinetic PIC result, and (c) and (c') is the collisional reduced PIC result. (b) and (d) are the collisionless simulation of (a) and (c), respectively. Plots (a)–(d) are observed at $t = 130$ fs, and (a') and (c') are at $t = 260$ fs. The contour level is ± 7 MG. (e) The electron energy spectrum observed at $t = 26$ fs in the target.

can be higher as a result of higher temperature in plasmas. In the reduced calculation, we need to pay attention whether the damping density is reasonably less than the n_{pic} .

Fig. 12 shows the quasi-static magnetic fields at 130 and 260 fs for both cases. Inside the target quasi-static magnetic fields grow due to an electromagnetic Weibel instability. Filaments reflect hot electrons and modify electron transport. There is a reasonable agreement between the fully resolved kinetic simulation and the reduced simulation, because collisions modify the Weibel instability scale length so that it is independent of the scale length of the pure kinetic instability and collisional physics is dominant. Plot (e) shows the electron energy spectrum inside the target. Again we see the very good agreement in the spectrum between the fully resolved PIC and reduced PIC.

Fig. 12b and d shows the magnetic fields at the same time as (a) and (c), but *without* collisions. The size of magnetic filaments appear inside the target in the reduced simulation is different from the ones in the full kinetic simulation. Since the reduced PIC simulation does not resolve the kinetic physics of the skin length scale in $160n_c$ plasmas (it has a resolution of $40n_c$ plasmas under the current set up), its result is meaningless without collisions.

6. Summary

We discuss numerical methods for relativistic particle simulations for large density gradients. This includes an advanced Coulomb collision model for large density scale plasma in wide particle energy range. Our model has perfect energy conservation in scattering and statistical momentum conservation. This is a great advantage to simulate HEDP with less number of particle per cell, still avoiding numerical energy violation, which is critical in HEDP problems. A relativistic collision operator is useful for relativistic particle transport physics in dense plasmas, like the fast ignition in the laser fusion or relativistic astrophysical jet transport in space. Benchmark simulations show the model validity in wide energy range with weighted particles. We also discuss a novel method that suppresses the growth of numerical instabilities in simulations where the skin length is not resolved. Comparisons with conventional PIC simulations show that this approach works.

Acknowledgements

Work supported by UNR under DOE/NNSA Grant DE-FC52-06NA27616 and DOE/OFES DE-PS02-07ER54837. This work was performed in part under the auspices of the US Department of Energy by Lawrence Livermore National Laboratory under Contract DE-AC52-07NA27344.

References

- [1] M. Tabak et al., Phys. Plasmas 1 (1994) 1626.
- [2] R. Shanny, J. Dawson, J.M. Greene, Phys. Fluids 10 (6) (1967) 1281.
- [3] T. Takizuka, H. Abe, J. Comput. Phys. 25 (1977) 205.
- [4] Y. Sentoku, K. Mima, Y. Kishimoto, M. Honda, J. Phys. Soc. Jpn. 67 (1998) 4084.
- [5] R.H. Miller, M.R. Combi, Geophys. Res. Lett. 21 (1994) 1735.
- [6] K. Nanbu, S. Yonemura, J. Comput. Phys. 145 (1998) 639.
- [7] C.K. Birdsall, A.B. Langdon, Plasma Physics via Computer Simulation, Institute of Physics, London, 1995.
- [8] J.D. Jackson, Classical Electrodynamics, John Wiley and Sons, New York, 1975.
- [9] E.M. Lifshitz, L.P. Pitaevskii, Physical Kinetics, Pergamon Press, Oxford, 1981 (Chapter 4).
- [10] L. Spitzer Jr., Physics of Fully Ionized Gases, Interscience, New York, 1956 (Chapter 5).
- [11] M. Lampe, Phys. Fluids 13 (1970) 2578.
- [12] Y.T. Lee, R.M. More, Phys. Fluids 27 (1984) 1273.
- [13] C.K. Birdsall, A.B. Langdon, Plasma Physics via Computer Simulation, Institute of Physics Publishing, Bristol/Philadelphia, 1991 (Chapter 4).
- [14] A.J. Kemp, Y. Sentoku, V. Sotnikov, S.C. Wilks, Phys. Rev. Lett. 97 (2006) 235001.
- [15] T. Johzaki, K. Mima, Y. Nakano, T. Yokota, H. Sumita, Fusion Sci. Technol. 43 (2003) 428.
- [16] T.Z. Esirkepov, Comput. Phys. Comm. 135 (2001) 14.